TOC

MnO$_2$@NiCo$_2$O$_4$ nanowire arrays on Ni foam were designed and developed as high-performance monolith de-NOx catalysts.

Journal Name

ARTICLE

Rational design and *in-situ* fabrication of MnO2@NiCo2O4 nanowire arrays on Ni foam as high-performance monolith de-NOx catalysts

Yan Liu‡, Jing Xu‡, Hongrui Li, Sixiang Cai, Hang Hu, Cheng Fang, Liyi Shi and Dengsong Zhang[*]

In this work, we have rationally designed and originally developed a novel monolith de-NOx catalyst with nickel foam as the carrier and three dimensional hierarchical $MnO_2@NiCo_2O_4$ core-shell nanowire arrays *in-situ* grown on the surface *via* a two-step hydrothermal process with a post calcination treatment. The catalysts were systematically examined by X-ray diffraction, scanning electron microscopy, transmission electron microscopy, elemental mapping, ion sputtering thinning, X-ray photoelectron spectroscopy, Inductively Coupled Plasma Atomic Emission Spectroscopy (ICP-AES), H_2 temperature-programmed reduction, $NH_3/NO+O_2$ temperature-programmed desorption measurements and catalytic performance tests. The results indicate that the nanowire is composed of hollow $NiCo_2O_4$ spinel as the core and MnO_2 nanoparticles as the shell layer. By ingeniously making the hierarchical Ni-Co oxides nanowires as the support of manganese oxides, $MnO_2@NiCo_2O_4@Ni$ foam catalyst not only takes the advantage of the high surface area of Ni-Co nanowires to achieve high loading amounts as well as high dispersion of manganese oxides, but also makes use of the synergistic catalytic effect between Ni, Co and Mn multiple oxides, and exhibits excellent low-temperature catalytic performance in the end. In addition, with the structure and morphology well maintained under the long term steady isothermal operation, the catalyst is able to sustain high NO conversion and exhibits superior catalytic cycle stability and good H_2O resistance. Considering all these favorable properties, the $MnO_2@NiCo_2O_4@Ni$ foam catalyst could be served as a promising candidate for the monolith de-NOx catalyst at low temperature and the rational design of *in-situ* synthesis of 3D hierarchical monolith catalyst also puts forward a new way for the development of environmental-friendly and highly active monolith de-NOx catalysts.

1. Introduction

Nitrogen oxides exhausted from automobiles and industrial combustion of coal and fossil fuel are not only highly toxic to human health but also have given rise to a variety of environmental and health-related issues, such as ozone depletion, photo chemical smog and acid rain.[1-3] Up to now, the selective catalytic reduction (SCR) with NH_3 as reducing agent is nowadays considered as the most promising technology for the elimination of NO_x.[4, 5] V_2O_5-WO_3 (MoO_3)/TiO_2 has been widely used as commercial catalysts for the NH_3-SCR of NO_x, which exhibit high catalytic activity and selectivity.[6, 7] Nevertheless, some inevitable disadvantages still remain, such as a high working temperature (300-400 °C),[8, 9] a narrow operating temperature window as well as the toxicity to the environment and human health.[10, 11] In this regard, it is extremely urgent to develop non-vanadium catalysts with a

highly catalytic activity for the NH_3-SCR application within low-temperature regions.[12-14]

For decades, some transition metal (e.g. Cr, Mn, Fe, Co, Ni, Cu) oxides and their composite oxides have been widely investigated in the low-temperature SCR reaction.[15-22] Among all these catalysts, manganese-containing catalysts including MnO_x–TiO_2,[23, 24] Fe-MnO_x,[25, 26] Ce-MnO_x[27, 28] and Co-MnO_x,[29, 30] have attracted lots of concerns due to their relatively high activity of removing NO_x at low temperature as well as their inherently environmentally benign character.

It is noted that in the practical application, the above-mentioned catalyst materials are usually loaded on the surface or mixed into the channel walls of ceramic monoliths or parallel passage reactors by wash coating, dip coating, impregnation or extrusion.[31-33] However, during the coating or impregnation process, the nanoparticles tend to aggregate, leading to the active species inhomogeneous. Besides, the low inter-phase heat transfer rate of ceramic honeycombs inevitably results in

the accumulation of ammonium salt in the corners of the channels.[34] All of these factors have a negative effect in the practical application of the catalysts. Therefore, it is of great challenge to develop high performance monolith catalysts with superior heat-mass transfer ability, highly dispersed active components and good structure stability.

In recent years, metal foam and wire mesh as new prospective catalyst carriers have aroused much concern for their high porosity, stability, thermal conductivity and the mass transfer ability.[35-37] Shu et al. reported a novel wire-mesh honeycomb catalyst for NH₃-SCR. The catalyst shows excellent catalytic activity and great resistance to H_2O, SO_2 and dust compared with ceramic honeycomb catalyst with the same components, attributed to the unique three-dimensional structure of the wire-mesh honeycomb which could inhibit the high sulfate-ammonium deposition on the surface of catalysts.[34] Yao et al. reported a wire-mesh honeycomb catalyst for SCR of NO with NH₃, and metal wire-mesh honeycomb catalyst shows broader temperature window and higher NO conversion than conventional ceramic honeycomb catalyst due to reduced mass transfer resistance by the existence of three dimensional holes in the metal wire mesh honeycomb.[38]

Three dimensional hierarchical nanostructures with many competitive advantages such as: short ion transport pathways, rich accessible electroactive sites, large specific area, good dispersion of all induced metal oxide species, favourable structure stability, efficient channels for mass transport, have been attracting sustained attention in the applications of supercapacitors,[39] lithium batteries,[40] catalysis,[41-43] solar cells and photocatalytic reactions.[44] In our early work,[35, 36] multi-metal oxides catalysts with the structure of 3D hierarchical nanosheets have been fabricated and exhibit improved catalytic behavior and excellent structure stability than the mixed oxides powders, attributed to the enhanced oxygen species, reducible species and acid sites exposed on the surface of catalysts. As a consequence, taking use of the relationship between the hierarchical structure and catalytic performance to fabricate catalysts is of great significance.

Herein, attracted by the advantageous catalytic performance of Mn, Ni and Co oxides species, favorable characters of metal foam as well as the unique three-dimensional hierarchical structure, we have rationally designed and in-situ fabricated hierarchical $MnO_2@NiCo_2O_4$ core-shell nanowire arrays on Ni foam as a novel monolith de-NOₓ catalyst for NH₃-SCR of NO, where the hollow $NiCo_2O_4$ nanowires are the ''core'' and MnO_2 nanoparticles are the ''shell'' layer. The synthetic route is schematically illustrated in Scheme1. As can be seen, the $MnO_2@NiCo_2O_4@Ni$ foam catalyst is fabricated via a two-step hydrothermal reaction coupled with a post calcination treatment. Firstly, the nanowire-like Ni-Co basic carbonate precursors are directly in-situ grown on nickel foam substrate via a urea assisted co-precipitated process based on the similar solubility product constant (K_{sp}) of Ni^{2+} ion and Co^{2+} ion, which also guarantees the homogeneous distribution of Ni and Co species within the precursors. Then, $MnO_2@Ni$-Co precursor nanowire arrays are obtained through the in-situ homogeneous precipitation of MnO_2 nanoparticles produced by the potassium permanganate pyrolysis on the surface of the exiting Ni-Co precursor nanowires, forming the nanoshell. Finally, the calcination procedure causes the formation of $MnO_2@NiCo_2O_4$ nanowire arrays. In this design, the MnO_2 nanoparticles anchored on the surface of Ni-Co nanowires, on the one hand, could provide an effective barrier to prevent the migration and agglomeration of metal oxides during the catalytic reaction. On

the other hand, the calcination procedure could give rise to the interaction between the inner $NiCoO_4$ and outer MnO_2, which is beneficial to the synergistic catalytic performance of catalysts. Considering the desirable properties of the three dimensional hierarchical structure and the Ni, Co and Mn multiple oxides, the $MnO_2@NiCo_2O_4@Ni$ foam catalyst may be served as a promising candidate for the monolith de-NOₓ catalyst at low temperature and the rational design of in-situ synthesis of 3D hierarchical monolith catalyst could also put forward a new way to develop environmental-friendly and high-activity monolith de-NOₓ catalysts.

2. Experimental Section

2.1 Catalysts preparation

All reagents were of analytical grade and used without further purification, supplied by Sinopharm Chemical Reagent Co. Ltd (China). Deionized water was used in the experiments. The nickel foam was purchased from Ailantian Advanced Technology Materials Co. Ltd (Dalian, China). Before use, the nickel foam was cut into small rounds(d = 20 mm, 1.6 mm thick) and pretreated with 0.1 M HCl aqueous solution upon ultrasonic vibration for 15 min to remove the grease and the possible surface oxide layer, and finally washed with deionized water to remove residual HCl.

In a typical synthesis, 4 mmol of $Ni(NO_3)_2·6H_2O$ and 8 mmol of $Co(NO_3)_2·6H_2O$ and 24 mmol of urea were dissolved in 80 mL of mixed solution with ethanol and H_2O (V:V=1:1) under stirring for 30 min. Subsequently, the cleaned nickel foams were immersed into the above mentioned homogeneous solution and then transferred to a 100 mL Teflon-lined stainless steel autoclave for 8 h of hydrothermal reaction under 110 °C. Then the autoclave was allowed to cool down naturally and the Ni foam was washed by deionized water upon ultrasonic vibration for 10 min to remove the surplus products and then dried in air at 70 °C. Secondly, 0.5 mmol of $KMnO_4$ was dissolved in 80 mL deionized water and then transferred into a 100 mL Teflon-lined stainless steel autoclave. After the as-prepared Ni foam was put into the solution, the autoclave was heated and maintained at 160 °C for 12h and then allowed to cool down to room temperature naturally. Finally the product was washed by deionized water upon ultrasonic vibration for 10 min, dried overnight and calcined in air at 500 °C for 4 h with a heating rate of 2 °C·min⁻¹.

In order to have a better understanding of the improved morphology and catalytic ability of the $MnO_2@NiCo_2O_4@Ni$ foam catalyst, $NiCo_2O_4@Ni$ foam, $MnO_2@Ni$ foam, MnO_2/Cordierite and NiO foam as reference samples were also fabricated via the similar route. The synthesis details can be found in ESI.

2.2 Catalyst characterization

The morphology and structure of the catalysts were characterized by scanning electron microscopy (SEM, JEOL JEM-200CX), transmission electron microscopy (TEM, JEOL JEM-200CX) and high-resolution TEM (HRTEM, JEOL JEM-2100F). Energy-dispersive X-ray (EDX) analysis and elemental mapping were conducted to obtain the component of the samples using an Inca Energy 200 TEM system from Oxford Instruments. Inductively Coupled Plasma Atomic Emission Spectroscopy (ICP-AES) analysis was conducted to obtain the contents of elements by the PERKINE 7300DV. The Powder

Journal Name

ARTICLE
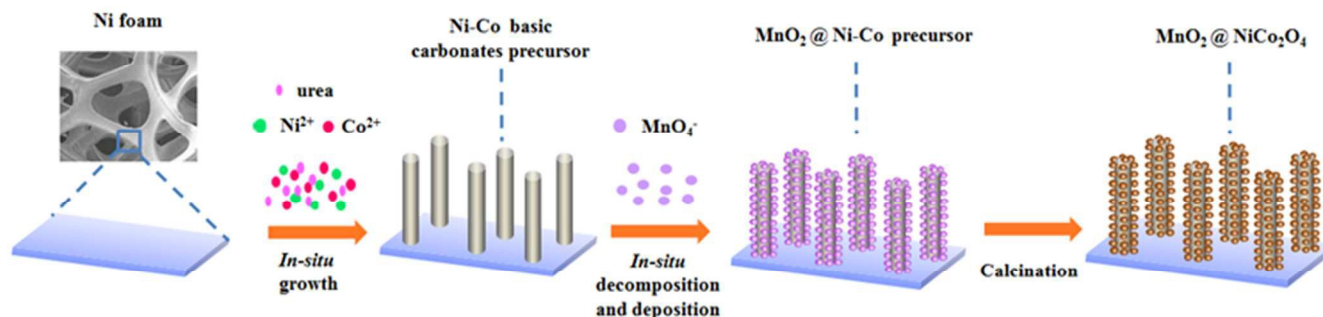
Scheme 1 Schematic illustration of the synthesis procedure of the $MnO_2@NiCo_2O_4@Ni$ foam.

X-ray diffraction (XRD) was measured by a Rigaku D/MAX-2200 X-ray diffractometer with Cu-Ka (40 kV, 40 mA) radiation and a secondary beam graphite monochromator. The diffraction data were collected over 2θ range of 10-90° with 0.02° intervals. The X-ray photoelectron spectroscopy (XPS) measurements were performed on a RBD upgraded PHI-5000C ESCA system with a hemispherical energy analyzer using an Mg-Ka (1253.6 eV) anode and a dual X-ray source. Before deconvolution, the binding energies refer to O, Ni Co and Mn were corrected according to contaminant carbon (C 1s = 284.6 eV) and the peak fitting was performed by using AugerScan (version 3.21) software. N_2 adsorption-desorption isotherms were obtained at 77 K using an ASAP 2020M Micromeritics. Before N_2 adsorption, the samples were degassed at 300 °C for 4 h. The specific surface areas were determined using the Brunauer-Emmett-Teller (BET) equation. Temperature-programmed reduction by hydrogen (H_2-TPR) was carried out on a Tianjin XQ TP5080 auto-adsorption apparatus. Before the reduction process, 80 mg of each catalyst was outgassed at 300 °C under N_2 flow for 30 min and then cooled down to room temperature. Afterwards, the reactor temperature was raised to 600 °C at a constant heating rate of 10 °C·min⁻¹ in H_2 (5 vol. %) /N_2 with a flow rate of 30 mL·min⁻¹ and the H_2 consumption data was recorded by a thermal conductivity detector (TCD). Temperature-programmed desorption experiments of ammonia (NH_3-TPD) were performed on the same Tianjin XQ TP5080 auto-adsorption apparatus and the desorption amounts of NH_3 was also monitored by the TCD. Prior to the experiments, 300 mg of catalysts were pretreated at 300 °C in a flow of He (30 mL min⁻¹) for 0.5 h and then cooled to 100 °C (under He protection). Subsequently, the samples were exposed to high-purity anhydrous ammonia at 100 °C for 90 min, followed by He purging for 1h. Finally, the temperature was raised from 100 to 700 °C in He flow at a ramping rate of 10 °C·min⁻¹. Temprature-programmed desorption experiments of $NO+O_2$ ($NO+O_2$-TPD) were conducted on a Tianjin XQ TP5080 auto-adsorption apparatus. Prior to the experiments, each sample was pretreated at 300 °C in a flow of He (30 mL min⁻¹) for 0.5 h and then cooled to room temperature (under He protection). Subsequently, the samples were exposed to a mixed gas containing 500 ppm NO and 5 vol. % O_2 with N_2 as the balance

at room temperature for 1 h, followed by He purging for 1h. Finally, the temperature was raised to 500 °C in He flow at a ramping rate of 10 °C·min⁻¹. The desorption amounts of NO_x was also monitored by the TCD. *In situ* diffuse reflectance infrared Fourier transform spectroscopy (*in situ* DRIFTS) experiments were performed on an FTIR spectrometer (Nicolet 6700) equipped with a Harrick DRIFT cell and an MCT/A detector cooled by liquid N_2. Before each experiment, the catalysts were pretreated at 300 °C in a flow of N_2 (50 mL·min⁻¹) for 0.5 h and then cooled down to room temperature under N_2 flow. Background spectra were recorded in the N_2 flow at different temperature and subtracted from each sample spectrum. All the *in situ* DRIFTS spectra were collected by accumulating 64 scans at a 4 cm⁻¹ resolution. For ammonia adsorption, the catalysts were treated in flow of 500 ppm NH_3 at room temperature for 1 h and then purged by N_2.

2.3 Catalyst performance tests

The NH_3-SCR activity tests were conducted in a fixed-bed quartz reactor (2 cm of internal diameter) operating in a steady state flow mode. Before test, the catalysts and 50 mg quartz wool (to avoid the axial diffusion) were inserted into the reactor. The reactant feed gas composition was list as follow: [NO] = [NH_3] = 500 ppm, [O_2] = 3 vol. %, [H_2O] = 8 vol. % (when used), N_2 as balance gas, the total flow rate was set as 215 mL min⁻¹ thus the gas hourly space velocity (GHSV) of 20,000 h⁻¹ was obtained. The SCR reaction was carried out in the temperature range from 50 to 300 °C and the data was recorded until the reaction reached a steady state. The concentrations of NO and NO_2 in the feed gases and the effluent streams were measured by a KM9106 flue gas analyzer. The concentrations NH_3 were measured by an IQ350 ammonia analyzer. The NO conversion was calculated according to the following expression：

$$\text{NO Conversion (\%)} = \frac{[NO]_{in} - [NO]_{out}}{[NO]_{in}} \times 100\% \qquad (1)$$

Where the $[NO]_{in}$ indicated the inlet NO concentration at steady-state; and the $[NO]_{out}$ indicated the sum concentration of outlet NO and NO_2.
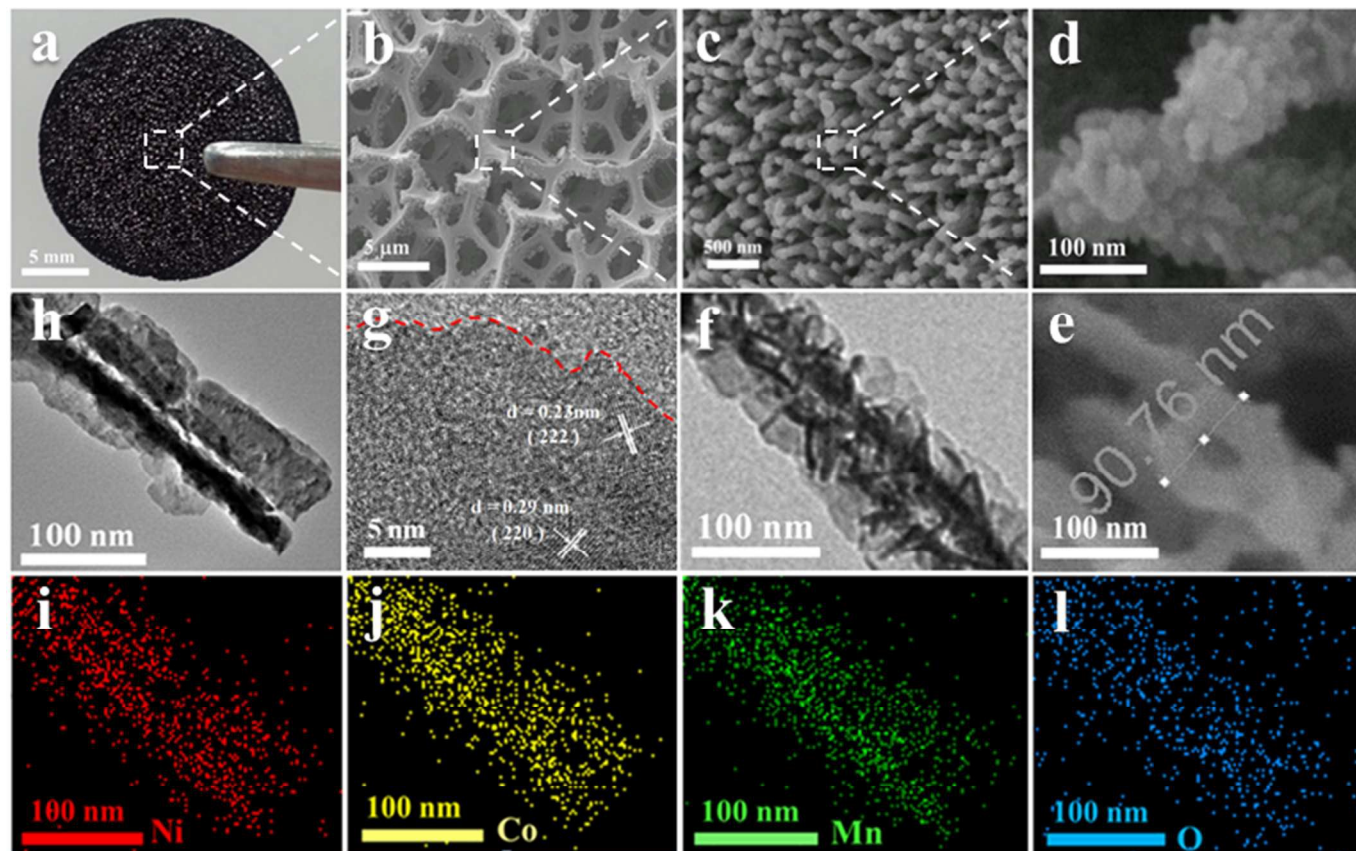
Journal Name

ARTICLE

Fig.1 (a) Optical photo, (b-d) SEM images of the $MnO_2@NiCo_2O_4@Ni$ foam; (e) SEM image of the $MnO_2@NiCo_2O_4@Ni$ foam after the ion sputtering thinning processing; (f) TEM image of the $MnO_2@NiCo_2O_4$ nanowire; (g) HRTEM image of the $MnO_2@NiCo_2O_4$ nanowire; (h-l) HAADF-STEM image and EDX-mapping images of the $MnO_2@NiCo_2O_4$ nanowire.

By assuming free of diffusion limitations, the SCR reaction rates normalized by the specific surface area of the catalyst can be calculated according to the following equation:[45, 46]

$$\text{rate (mol} \cdot m^{-2} \cdot s^{-1}) = \frac{X_{NO}QC_f}{V_m WS_{BET}} \quad (2)$$

Where X_{NO} is the NO conversion at a steady SCR reaction temperature (50-175 ^{o}C at 25 ^{o}C intervals) (%), Q is the volumetric flow rate (750 ml/min) and C_f is the feeding concentration of NO (500 ppm). V_m is the molar volume of gas (22.4 ml/mole), W is the catalyst weight (g) and S_{BET} is the specific area of the catalyst (m^2/g). The apparent activation energy for SCR reaction was determined by the slope of the plot.

In order to parallelly compare the activities of different catalysts, a relative turn over frequency (TOF) value was employed. The relative TOF (s^{-1}) of NO over per Mn atom was calculated by the following equation: [8, 47]

$$\text{TOF} = \frac{(P\upsilon/RT)\,\alpha}{m_{cat}\beta_{Mn}/M_{Mn}} \quad (3)$$

Where P was the standard atmospheric pressure (1.01×10^5 Pa); υ was the flow rate of NO (0.24 mL min^{-1}); R was the proportional constant (8.314 J mol^{-1}K^{-1}); T was the room temperature (298K); α was the NO conversion of the catalysts at the steady SCR reaction temperature (%); m_{cat} was the mass of the catalysts ($MnO_2@NiCo_2O_4@Ni$ foam is 2.109 g, $MnO_2@Ni$ foam is 1.885 g); β_{Mn} was the Mn loading calculated from ICP (%); and M_{Mn} was the molar mass of Mn (54.9 g mol^{-1}). Based on the NO conversion at 50 ^{o}C, the TOF for the $MnO_2@NiCo_2O_4@Ni$ foam and $MnO_2@Ni$ foam were calculated using the above equation.

3. Results and discussion

3.1 Morphology and structure of the catalysts

The morphology and structure of the $MnO_2@NiCo_2O_4$ @Ni foam were studied by SEM and TEM. The nickel foam with the three-dimensional transparent framework exhibits a flat surface

(Fig S1, ESI), which could serve as the support and growth center of the MnO$_2$@NiCo$_2$O$_4$ nanowires. Fig. 1a-b shows that after the hydrothermal reaction and calcination treatment to *in-situ* grow MnO$_2$@NiCo$_2$O$_4$ nanowire arrays on the surface, the nickel foam well maintains the three-dimensional net structure. Fig. 1c shows that the MnO$_2$@NiCo$_2$O$_4$ nanowires are uniformly grown on the nickel foam on a large scale forming a new three-dimensional hierarchical structure, and the nanowires are homogeneously aligned and separated apart adequately. The high-magnification SEM image (Fig. 1d) clearly reveals that the surface layer of each nanowire is made up of numerous small nanoparticles, and the nanowire is about 100 nm in diameter and 600-700 nm in length. A similar morphology can be observed on the Ni-Co basic carbonate precursors (Fig. S3 a-b, ESI), suggesting that the well-defined array structure is well retained and MnO$_2$ nanoparticles preferentially *in-situ* deposit on the surface of Ni-Co nanowires and forms the uniform coverage. The EDS spectrum (Fig. S2b, ESI) of the MnO$_2$@NiCo$_2$O$_4$ nanowires also confirms that the NiCo$_2$O$_4$ nanowires have been coated by the MnO$_2$ layers. In the meantime, the reference sample MnO$_2$@Ni foam was also prepared by directly deposit MnO$_2$ species on the surface of Ni foam. The SEM images (Fig. S4c-b, ESI) suggest that there is a low loading of manganite oxides on the Ni foam and the MnO$_2$ species are inhomogeneous, which further indicates that the Ni-Co nanowire is a good carrier of MnO$_2$ species and the unique hierarchical structure of nanowires providing more specific area for the deposition of MnO$_2$. Simultaneously, such a unique structure of catalysts can also expose abundant effective reactive sites, so that more gas molecules could participate in the reaction. Besides, the open and free interspaces among these nanowires will also help facilitating the transmission and diffusion of reactant gas molecules. So, it is believed that the 3D hierarchically structure is beneficial to the catalytic process.

More detailed structural information and morphology evolution of the MnO$_2$@NiCo$_2$O$_4$ nanowires were further investigated by TEM, HRTEM and SEM after ion sputtering thinning process. The SEM images (Fig. 1e, Fig. S5, ESI) of the MnO$_2$@NiCo$_2$O$_4$ nanowire arrays after the ion sputtering thinning process show that the hollow structure is about 30 nm in diameter. Fig. 1f evidently reveals that the MnO$_2$@NiCo$_2$O$_4$ nanowire is straight with an average diameter of 100 nm in accord with SEM images, and MnO$_2$@NiCo$_2$O$_4$ nanowire

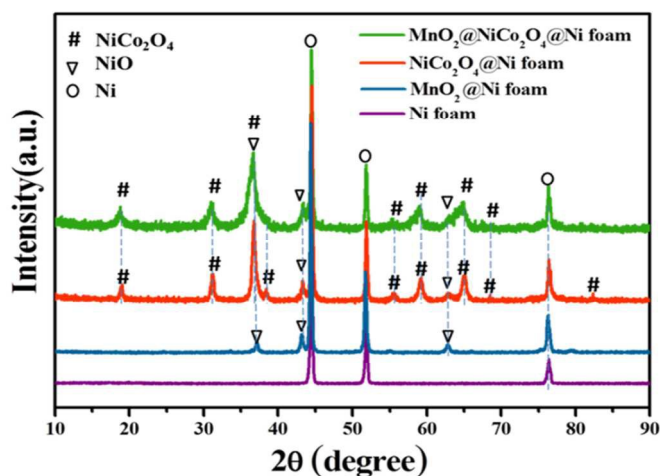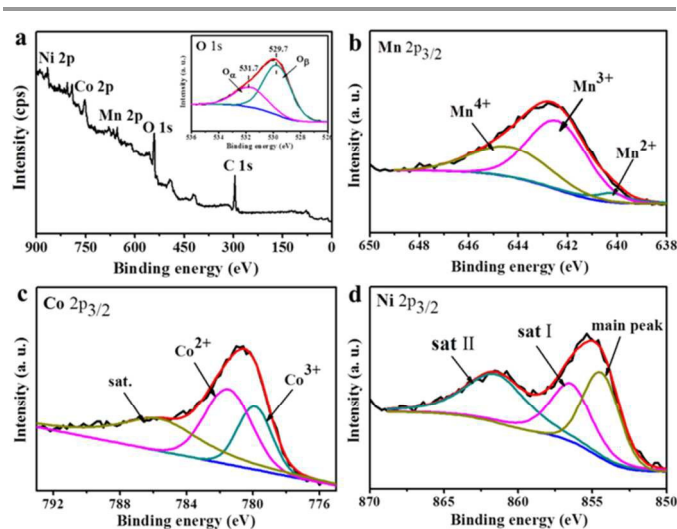Fig.3 (a) XPS spectra of MnO$_2$@NiCo$_2$O$_4$ nanowire and O 1s XPS spectra (inset); (b-d) XPS survey scan of Mn 2p, Co 2p and Ni 2p regions, respectively.

shows a typical hollow core-shell architecture with NiCo$_2$O$_4$ nanowire, about 60 nm in diameter, as the core and MnO$_2$ nanoparticles, about 20 nm in thickness, as the shell layer, consistent with the above results. The HRTEM image of MnO$_2$@NiCo$_2$O$_4$ nanowire (Fig. 1g) reveals that the *d*-spacing of 0.23 and 0.29 nm corresponds to the distance of the (222) and (220) planes, respectively, of the NiCo$_2$O$_4$ crystal (JCPDS card no. 20-0781), and the amorphous regions correspond to MnO$_2$. It is generally accepted that the dispersion of active components has crucial relationship with the catalytic activity.[29, 48] Therefore, the elemental mapping was performed to illustrate the chemical components and the spatial distribution of the corresponding elements in the MnO$_2$@NiCo$_2$O$_4$ nanowires, as shown in Fig. 1h-l. The EDS mapping results unambiguously confirm the well-defined MnO$_2$@NiCo$_2$O$_4$ core-shell nanowire structure with the Ni, Co, O, and Mn atoms uniformly distributed within the whole nanowire. Taking a careful observation, the distribution range of Mn is the same as those of Ni and Co, demonstrating that the MnO$_2$ uniformly covers the NiCo$_2$O$_4$.

The overall crystal structure and phase purity of the MnO$_2$@NiCo$_2$O$_4$@Ni foam catalyst and reference samples were verified by the XRD. We scratched the active components from the nickel foam to reduce the impact of the substrate on the XRD peak signals. The obtained patterns of the samples are shown in Fig. 2. The diffraction peaks at 18.9, 31.14, 36.69, 44.62, 55.44, 59.09, 64.98° are ascribed to the characteristic reflections of spinel NiCo$_2$O$_4$ (JCPDS card no. 20-0781).[49] The diffraction peaks at 43.28, 62.85° are ascribed to the characteristic reflections of NiO (JCPDS card no. 44-1159). The three strong and sharp peaks marked by "O" belong to the Ni substrate. No characteristic diffraction peaks of manganese oxide species can be detected in the XRD profiles, which could be attributed to the amorphous manganese oxides.

The XPS studies were also conducted to determine the chemical composition and element chemical state on the surface of MnO$_2$@NiCo$_2$O$_4$@Ni foam. Fig. 3a shows the presence of O, Mn, Co, Ni elements within nanowire, consistent with the results of EDS and element mapping. Fig. 3(a-d) show the XPS survey scan of O 1s, Mn 2p, Co 2p and Ni 2p regions, respectively. The XPS spectra of O 1s (Fig.3a) could be fitted into two peaks denoted as O$_\alpha$ and O$_\beta$. Normally,

Fig.2 XRD pattern of the MnO$_2$@NiCo$_2$O$_4$@Ni foam and the reference samples.

the peak located at 531.3-532 eV (denoted as O_α) is the characteristic peak of surface-absorbed oxygen from the oxide defects or hydroxyl groups, and the other centered at 529.6-530.1 eV is ascribed as lattice oxygen.[50] The abundance of O_α in $MnO_2@NiCo_2O_4@Ni$ foam may be beneficial to the NH_3-SCR of NO.[50] The Mn $2p_{3/2}$ spectra (Fig. 3b) is divided into three characteristic peaks attributed to Mn^{2+} (640.4 eV), Mn^{3+} (642.0 eV) and Mn^{4+} (644.1 eV), respectively.[51] And the Mn^{4+} and Mn^{3+} are the dominant valance states. It is accepted that Mn^{4+} has a strong oxidation reduction ability, which might promote "fast SCR" reaction attributed to the enhancement of NO oxidation to NO_2. Meanwhile, Mn^{3+} is the intermediate valence which has a great transforming ability between various valance states of Mn species, and in consequence it could promote the redox cycle during the catalytic process.[13, 29, 36] The high content of Mn^{4+} and Mn^{3+} might play an important role in the NH_3-SCR reaction at low temperature. The Co $2p_{3/2}$ spectra (Fig. 3c) is fitted into two peaks at 779.9 eV and 781.5 eV, assigned to Co^{3+} and Co^{2+} respectively.[29] It is reported that Co^{3+} species are prior for oxidation cycle within various valence state of cobalt and beneficial to NH_3 chemisorption,[52] so that Co^{3+} species could enhance the catalytic activity. Fig. 3d shows the Ni $2p_{3/2}$ spectra. The peaks located at 861.5 eV, 856.5 eV and 854.4 eV are assigned to two satellite peaks (denoted as Sat I and Sat II) and the main peak of Ni $2p_{3/2}$, respectively. The Sat I peak is corresponding to the Ni^{3+}, Ni^{2+}-OH or Ni^{2+} vacancies.[36, 53] According to the results of XPS, the abundance of oxide defects, active Mn^{4+}, Mn^{3+}, Ni^{3+} and Co^{3+} on the surface of $MnO_2@NiCo_2O_4@Ni$ foam catalyst is beneficial to the NH_3-SCR performance.

3.2 Physicochemical property of the catalysts

The H_2-TPR analyses were employed to evaluate the oxidation-reduction properties of the catalysts. The TPR profiles of $MnO_2@NiCo_2O_4@Ni$ foam, $NiCo_2O_4@Ni$ foam, $MnO_2@Ni$ foam and NiO foam are shown in Fig. 4a, respectively. As can be seen, all of the samples show a main reduction peak in the lower temperature regions. The NiO foam shows a well-defined reduction peak centered at 348 °C, which is corresponding to the reduction of Ni species from Ni^{2+} to Ni. Compared with NiO foam, after coated by MnO_2 or $NiCo_2O_4$ oxide layer, the H_2 consumption peaks of both $MnO_2@Ni$ foam and $NiCo_2O_4@Ni$ foam shift slightly to the lower temperature regions (located at 327 °C and 335 °C, respectively), indicating the improved redox ability. In the case of $MnO_2@NiCo_2O_4@Ni$ foam, a strong reduction peak located at 328 °C and a broad weak peak in the temperature range of 400-500 °C are observed. This reduction profile is the superposition of reduction peaks of nickel, cobalt and manganese oxides. As the area of the reductive peak, on behalf of the H_2 consumption, is related to the amount of reducible species, the $NiCo_2O_4@Ni$ foam reveals the largest reduction peak area compared with $MnO_2@Ni$ foam and NiO foam, which could be attributed to the rich Ni-Co redox species as well as the large surface area provided by the unique hierarchical nanowires array (Fig. S4, ESI). The appearance of new reduction peak at 440 °C in the profile of $MnO_2@NiCo_2O_4@Ni$ foam, which is the typical reduction of Mn_3O_4 to MnO, [51, 54] demonstrates that there are abundant manganese oxides on the surface of the catalyst, and this may be due to that the unique hierarchical structure of Ni-Co nanowires provide large specific areas and makes it easier to deposit more manganese oxides on the surface. It has been reported that the redox property of catalysts is remarkably related to the catalytic cycle in NH_3-SCR of NO, so more
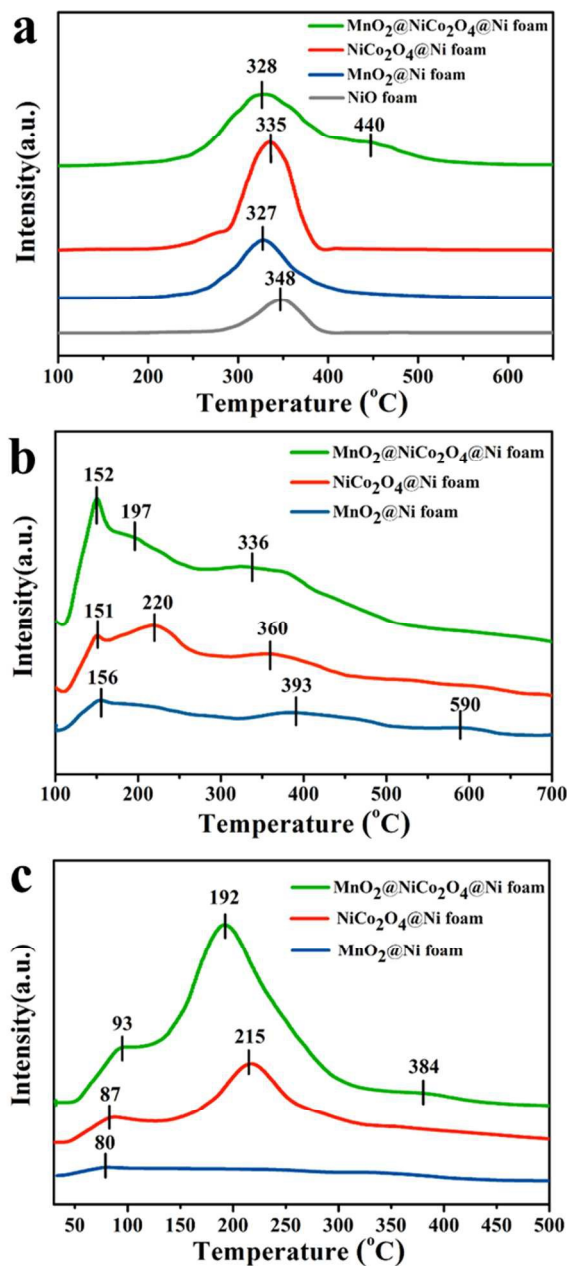

Fig.4 Physicochemical property of the $MnO_2@NiCo_2O_4@Ni$ foam catalyst and the reference samples: a) H_2-TPR profiles; b) NH_3-TPD profiles; c) $NO+O_2$-TPD profiles.

reducible species and better redox ability of the $MnO_2@NiCo_2O_4@Ni$ foam may be favorable for increasing the catalytic activity.

Based on the mechanism of NH_3-SCR of NO at low temperature, it is generally believed that the adsorption and activation of NH_3 on the surface acid sites of the catalysts is a key process in the NH_3-SCR with NO at low temperature. Therefore, the NH_3-TPD measurement was performed to investigate the surface acid distribution and amount of the catalysts, as depicted in Fig. 4b. The TPD profile of $MnO_2@Ni$ foam shows three weak and broad desorption peaks centered at 156, 393 and 590 °C, indicating that the absorption of NH_3 is weak, which may results from the low loading of manganite oxide on the Ni foam. As for $NiCo_2O_4@Ni$ foam, the TPD

profile displays three instinct desorption peaks loaded at 151, 220 and 360 °C, respectively, and the area of the adsorption peaks increases apparently. Furthermore, in the case of $MnO_2@NiCo_2O_4@Ni$ foam, a strong sharp peak at 152 °C, two broad peaks centered at 197 and 336 °C are observed. What's more, the area of the reduction peaks is obviously the largest among the three catalysts. It has been demonstrated that the position of desorption peak is closely related to the strength of the acid sites of catalysts, and the peak area corresponds to the adsorption amount of NH_3. Since the NH_4^+ ions bound to Brønsted acid sites are less thermally stable than coordinated NH_3 molecules bound to Lewis acid sites and desorb at lower temperature, it can be deduced that the low-temperature peak is assigned to NH_4^+ ions bound to the Brønsted acid sites and the desorption peak at high temperature is associated with coordinated NH_3 molecules from the Lewis acid site.[29, 55] According to the result of the *in situ* DRIFTS of NH_3 adsorption (Fig. S6, ESI), there are both Brønsted acid sites and Lewis acid sites on the surface of the $MnO_2@NiCo_2O_4@Ni$ foam catalyst. So, the strong and sharp desorption peak at about 152 °C existed in all catalysts can be assigned to the NH_3 desorbed by weak Brønsted acid sites on the catalysts surface. The peak in the temperature range of 200-400 °C is corresponding to the weak Lewis acid sites, and the desorption peak at 400-600 °C is the contribution of NH_3 desorbing from the medium acid sites in the catalysts. Comparatively, the $MnO_2@NiCo_2O_4@Ni$ foam has the similar acid sites distribution with $NiCo_2O_4@Ni$ foam. According to the literatures, the weak acid site is beneficial to the adsorption and activation of NH_3. While, after MnO_2 nanoparticles deposit on the surface of the Ni-Co nanowires forming the nanoshells, the areas of the desorption peaks, especially the peak at 152 °C increase remarkably, demonstrating an advanced adsorption of reactant ammonia molecules. Simultaneously, the desorption peaks at 220 and 360 °C move to a lower temperature region at 197 and 336 °C, respectively, revealing an easier adsorption ability of NH_3. In this regard, with the Ni-Co oxides nanowire as the support, and the reactive Mn nanoparticles *in-situ* depositing on its surface, the $MnO_2@NiCo_2O_4@Ni$ foam catalyst brings about high effective specific surface area so that more acid sites could be exposed, and exhibits enhanced adsorption ability of NH_3 due to the synergistic effect of multiple oxides.

To further investigate the adsorption behavior of NO_x on the surface of catalysts, the $NO+O_2$-TPD measurement was also conducted, as depicted in Fig.4c. The TPD profile of $MnO_2@Ni$ foam shows a very weak and broad peak, and both $MnO_2@NiCo_2O_4@Ni$ foam and $NiCo_2O_4@Ni$ foam show distinct peaks located at 93, 192, 384 °C and 87, 215 °C, respectively. According to reports, the desorption peak at approximately 100 °C represented the physical adsorption and weak chemisorption of NO, the desorption peak located below 300 °C could be attributed to the desorption of monodentate nitrites or nitrates, whereas, the peak at temperatures greater than 300 °C is caused by the decomposition of strongly coordinated species, such as bidentate or bridging nitrates.[50, 56] Accordingly, the NO adsorption over $MnO_2@Ni$ foam is much weaker in contrast to the $MnO_2@NiCo_2O_4@Ni$ foam and $NiCo_2O_4@Ni$ foam, which may be attributed to the limitation of specific surface area and the lesser loads on Ni foam. While, in the case of $NiCo_2O_4@Ni$ foam, the lower temperature desorption peak at 87 °C belongs to the physical adsorbed NO, and the peak at 215 °C corresponds to the desorptions of monodentate nitrites or nitrates. The much larger peak area

suggests that the bigger specific surface area of Ni-Co nanowire can provide more basic sites to adsorb NO. By contrast, it is interesting to find that after the coverage of MnO_2, the adsorption peaks at 87 °C shift to 93 °C with increased area, and the middle temperature peak at 215 °C shifts to lower temperature by about 23 °C, and a new weak desorption peak at 384 °C emerges, demonstrating that the introduction of MnO_2 not only significantly increases the amount of adsorption sites of the catalyst, but also makes it easier to adsorb NO as the adsorption temperature decreases. In addition, the adsorption ability of the catalyst becomes stronger, which could be the result of the interaction between the Ni-Co oxides and Mn species. The various adsorption species detected in the *in situ* DRIFTS of $NO+O_2$ adsorption (Fig. S7, ESI) further confirms that the $MnO_2@NiCo_2O_4@Ni$ foam catalyst has a great ability of chemisorption and activation of reactant molecules. As the adsorption capacity of NO is of great importance in the NH_3-SCR reaction at low temperature, so the difference in the absorbability of NO of $MnO_2@NiCo_2O_4@Ni$ foam catalyst and its reference samples may give rise to the distinction of the catalytic performance.

Taking the above H_2-TPR, NH_3-TPD and $NO+O_2$-TPD results into consideration, it is not difficult to find that the enhanced surface areas as a result of the dimensional hierarchical nanowire arrays bring about more reductive species and help to absorb more reactant molecules both NO and NH_3. Moreover, the synergistic effect of multiple oxides contributes to physicochemical properties of the catalyst, resulting in better catalytic performance.[8, 36, 51, 57] All these effects could lead to the promotion of the activity of catalysts for NH_3-SCR of NO at low temperature.

3.3 Catalytic performance

The NH_3-SCR activity measurements as a function of temperature from 50 °C to 300 °C of $MnO_2@NiCo_2O_4@Ni$ foam, $NiCo_2O_4@Ni$ foam, $MnO_2@Ni$ foam, MnO_2/Cordierite and Ni foam were carried out, and the corresponding catalytic performance is depicted in Fig. 5a. It is found that, as the catalyst carrier, the nickel foam itself hardly shows catalytic ability during the whole temperature range except at higher temperature (> 200 °C), which is benefited from the active nickel oxide species forming on the surface of nickel foam at high temperature (Fig. S8, ESI). After decorated by the $NiCo_2$-O_4 nanowire arrays, the $NiCo_2O_4@Ni$ foam exhibits a much better catalytic ability within a narrow temperature region from 150 °C to 250 °C and the maximum NO conversion (ca. 50 %) is achieved at 200 °C. As for $MnO_2@Ni$ foam, it is notable to detect that with the increasing of temperature, the NO conversion increases rapidly from 125 °C to 250 °C and reaches the maximum NO conversion of 96 % at 225 °C at GHSV 20,000 h^{-1}, and the light-off temperature of NO (T_{50}) is at about 175 °C. And in the case of $MnO_2@NiCo_2O_4@Ni$ foam, it shows enhanced catalytic activity at low temperature with its T_{50} reaching at 80 °C, much lower than that of both $NiCo_2$-$O_4@Ni$ foam and $MnO_2@Ni$ foam, and the temperature window for NO conversion more than at GHSV 20,000 h^{-1}, lasting for nearly 100 °C (from 127 to 227 °C). Making these three catalysts a comparison, it can be deduced that MnO_2 is a main active component in the NH_3-SCR of NO, and the hierarchical Ni-Co nanowire is a favorable carrier of manganese oxides for improving its loading amounts and dispersion (Tab. 1, ESI). The excellent performance over $MnO_2@NiCo_2O_4@Ni$ foam could be attributed to the unique

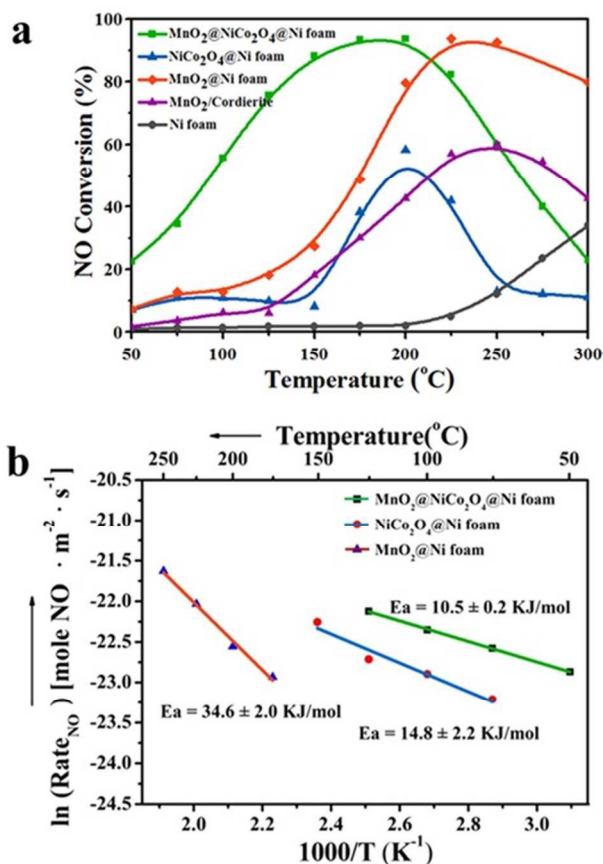**Fig.5** (a) NH$_3$-SCR performance as a function of temperature. Reaction conditions: [NO] = [NH$_3$] = 500 ppm, [O$_2$] = 3 vol. %, N$_2$ as balance gas, and GHSV = 20,000 h^{-1}. (b) Arrhenius plots of the SCR reaction rates of catalysts at 50–175 °C. Conditions: [NO] = [NH$_3$] = 500 ppm, [O$_2$] = 3 vol. %, N$_2$ as balance gas, and GHSV = 60,000 h^{-1}.

structure, large specific areas and active components. Firstly, the hierarchical structure is in favor of the transmission and diffusion of reactant gas molecules, which play an important role in the NH$_3$-SCR reaction, and the hierarchical structure brings about highly uniform distribution of Ni, Co and Mn oxide species within the nanowires, efficiently inhibiting the aggregation of active components. Then, MnO$_2$@NiCo$_2$O$_4$@Ni foam with high specific areas (Tab. 2, ESI) can expose more redox species and adsorption sites, so that more NO and NH$_3$ molecules could participate in the reaction. Furthermore, the synergistic catalytic effect between Ni, Co and Mn multiple oxides also contributes to the catalytic behaviour. As for MnO$_2$@Ni foam and MnO$_2$/Cordierite, the MnO$_2$@Ni foam shows higher NO conversion during the whole temperature region than MnO$_2$/Cordierite, indicating that Ni foam is a favorable carrier for monolith catalysts due to its high porosity, mass transfer ability, thermal conductivity as well as the possible interaction between the substrate Ni and surface Mn species.

We also estimated the relative TOF of NO over per Mn atom for MnO$_2$@NiCo$_2$O$_4$@Ni foam and MnO$_2$@Ni foam at 50 °C. The result shows that the TOF value of MnO$_2$@NiCo$_2$O$_4$@Ni foam (0.52 × 10^{-4} s^{-1}) is much higher than that of MnO$_2$@Ni foam (0.43 × 10^{-4} s^{-1}). It seems that the hierarchical MnO$_2$@NiCo$_2$O$_4$ nanowires exhibited better activity, which is probably attributed to the interactions among Mn，Ni and Co
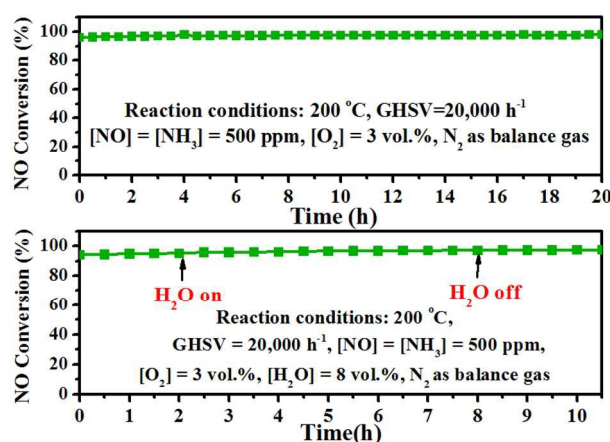

Fig.6 Stability and H$_2$O resistance test at 200 °C of the MnO$_2$@NiCo$_2$O$_4$@Ni foam catalyst.

oxides and the specific structures.[47]

The SCR reaction rates of NO over per square meter catalysts were calculated according to Eq. 2 under appropriate reaction condition, where the NO conversion is less than 30% (Fig. S10). Fig. 5b shows the Arrhenius plots based on the reaction rates between the temperature regions. As for MnO$_2$@NiCo$_2$O$_4$@Ni foam, the apparent activation energy is 10.5 ± 0.2 KJ/mol, which is much lower than that of NiCo$_2$O$_4$@Ni foam (14.8 ± 2.2 KJ/mol) and MnO$_2$@Ni foam (34.6 ± 2.0 KJ/mol), indicating that MnO$_2$@NiCo$_2$O$_4$@Ni foam needs less energy than NiCo$_2$O$_4$@Ni foam and MnO$_2$@Ni foam for the reaction, so that it has the highest catalytic activity.

The catalytic stability is of great importance in practical applications for the catalyst, so we evaluate the catalytic stability of the MnO$_2$@NiCo$_2$O$_4$@Ni foam, and the result is depicted in Fig. 6. The test was carried out at 200 °C and lasted for 20 hours without interruption. As can be seen, during the whole test period, the NO conversion is maintained at ca. 97 % at GHSV 20,000 h^{-1}, revealing the superior catalytic stability. To better understand the good catalytic stability, the SEM and XRD measurement of the catalyst after the stability test were conducted. The SEM image in Fig. 7a shows that the morphology of the catalyst keeps unchanged without any damage or deposition of ammonium salts, so that the active sites are able to fully expose. The XRD pattern in Fig. 7b shows that the chemical composition and phase structure of the catalyst retain well. Therefore, it is reasonable to deduce that the excellent stability of morphology and structure ensure the catalytic stability in NH$_3$-SCR.

In addition, as there is always some residual H$_2$O in the exhaust fume, which can poison and deactivate the catalyst by inhibition the active sites,[47, 58] the H$_2$O resistance test at 200 °C with the presence of 8 vol. % H$_2$O in the feed gas was conducted to test the impact of H$_2$O on the SCR activity of the MnO$_2$@NiCo$_2$O$_4$@Ni foam catalyst. As shown in Fig. 6, the NO conversion is not affected by H$_2$O and keeps at ca. 96 % as initial during the test. As is reported, the main deactivation of the catalyst in the H$_2$O containing NH$_3$-SCR test is the competitive absorption of H$_2$O with NH$_3$ molecules on the active sites of the catalyst. So the remarkable H$_2$O-resisitance ability of the catalysts may be ascribed to the strong adsorption of NH$_3$ on the abundant weak and middle acid sites of the catalyst, as has been demonstrated in NH$_3$-TPD experiments.
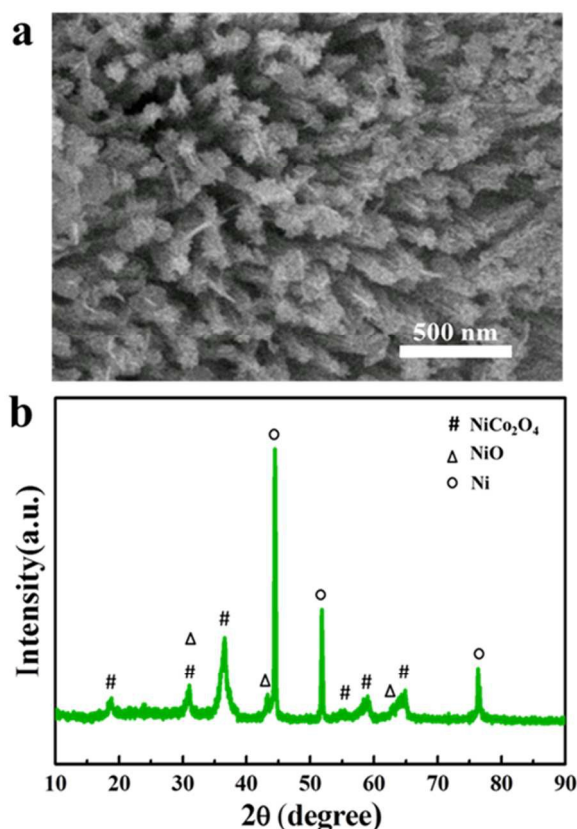
Fig.7 (a) SEM image and (b) XRD pattern of the MnO$_2$@NiCo$_2$O$_4$@Ni foam catalyst after the stability test.

4. Conclusions

In summary, we have rationally designed and *in-situ* fabricated the hierarchical MnO$_2$@NiCo$_2$O$_4$ @Ni foam with three dimensional hierarchical core-shell nanowire arrays on Ni foam as monolith de-NOx catalyst *via* a facile two-step hydrothermal process and a post calcination treatment. The MnO$_2$@NiCo$_2$O$_4$@Ni foam catalyst displays an enhanced low-temperature NH$_3$-SCR activity compared with the NiCo$_2$O$_4$@Ni foam, MnO$_2$@Ni foam, and MnO$_2$@cordierite, with the maximum NO conversion of 96 % at 175 ^{o}C and keeping above 80 % NO conversion at GHSV 20,000 h^{-1} within the broad temperature window from 127 to 227 ^{o}C. Such favorable catalytic behavior is attributed to the enriched active sites, reducible species, and acid sites exposed on the large accessible specific surface of the 3D hierarchical core-shell nanowire arrays as well as the synergistic catalytic contribution from Ni, Co and Mn oxides. In addition, the *in-situ* fabrication of monolith catalyst not only avoids the use of adhesive, preventing pollution, but also brings about a strong adhesion between active components and support, leading to the structure and morphology stability.[35] Simultaneously, the high porosity, thermal conductivity and mass transfer ability of nickel foam could also contribute to the transmission and diffusion of gas molecules. Considering all these favourable properties of the unique hierarchical structure and the multiple oxides, the MnO$_2$@NiCo$_2$O$_4$@Ni foam catalyst may be served as a promising candidate for the monolith de-NO$_x$ catalyst at low temperature and the rational design of *in-situ* synthesis of

3D hierarchical monolith catalyst also puts forward a new way for the development of environmental-friendly and high-activity monolith de-NO$_x$ catalyst.

Notes and references

Research Center of Nano Science and Technology, School of Material Science and Engineering, Shanghai University, Shanghai 200444, China. Fax: +86-21-66136079; Tel: +86-21-66136081; E-mail: dszhang@shu.edu.cn

† Electronic Supplementary Information (ESI) available: experimental details of NiCo$_2$O$_4$@Ni foam, MnO$_2$@Ni foam, NiO foam and MnO$_2$/Cordierite; SEM image and EDX spectrum of the MnO$_2$@NiCo$_2$O$_4$ nanowires; SEM image and TEM image of the Ni-Co basic carbonates precursor; SEM images of NiCo$_2$O$_4$@Ni foam, MnO$_2$@Ni foam and NiO foam; SEM image of the MnO$_2$@NiCo$_2$O$_4$@Ni foam after the ion sputtering thinning; *in situ* DRIFTS of NH$_3$/NO+O$_2$ adsorption on MnO$_2$@NiCo$_2$O$_4$@Ni foam; NH$_3$-SCR performance of NiO foam; surface areas, ICP-AES and EDX analysis of the monolith MnO$_2$@NiCo$_2$O$_4$@Ni foam and the reference samples; NO$_2$ concentration of MnO$_2$@NiCo$_2$O$_4$@Ni foam during the SCR reaction; NH$_3$-SCR performance as a function of temperature with GHSV = 60,000 h^{-1}. See DOI: 10.1039/b000000x/

‡These authors contributed equally to this work.

1. P. Forzatti, I. Nova and E. Tronconi, *Angew. Chem. Int. Ed.*, 2009, **121**, 8516-8518.
2. S. Beirle, K. F. Boersma, U. Platt, M. G. Lawrence and T. Wagner, *Science*, 2011, **333**, 1737-1739.
3. Y. Li, H. Cheng, D. Y. Li, Y. S. Qin, Y. M. Xie and S. D. Wang, *Chem. Commun.*, 2008, 1470-1472.
4. J. H. Li, R. H. Zhu, Y. S. Cheng, C. K. Lambert and R. T. Yang, *Environ. Sci. Technol.*, 2010, **44**, 1799-1805.
5. P. Li, Y. Xin, Q. Li, Z. P. Wang, Z. L. Zhang and L. R. Zheng, *Environ. Sci. Technol.*, 2012, **46**, 9600-9605.
6. I. Nova, L. Lietti, L. Casagrande, L. Dall'Acqua, E. Giamello and P. Forzatti, *Appl. Catal., B*, 1998, **17**, 245-258.
7. L. Lietti, P. Forzatti and F. Berti, *Catal. Lett.*, 1996, **41**, 35-39.
8. R. H. Gao, D. S. Zhang, X. G. Liu, L. Y. Shi, P. Maitarad, H. R. Li, J. P. Zhang and W. G. Cao, *Catal. Sci. Technol.*, 2013, **3**, 191-199.
9. J. H. Li, H. Z. Chang, L. Ma, J. M. Hao and R. T. Yang, *Catal. Today*, 2011, **175**, 147-156.
10. P. Balle, B. Geiger and S. Kureti, *Appl. Catal., B*, 2009, **85**, 109-119.
11. D. M. Chapman, *Appl. Catal., A*, 2011, **392**, 143-150.

12. Y. P. Wan, W. R. Zhao, Y. Tang, L. Li, H. J. Wang, Y. L. Cui, J. L. Gu, Y. S. Li and J. L. Shi, *Appl. Catal., B*, 2014, **148**, 114-122.

13. C. Fang, D. S. Zhang, S. X. Cai, L. Zhang, L. Huang, H. R. Li, P. Maitarad, L. Y. Shi, R. H. Gao and J. P. Zhang, *Nanoscale*, 2013, **5**, 9199-9207.

14. M. F. Fu, C. T. Li, P. Lu, L. Qu, M. Y. Zhang, Y. Zhou, M. G. Yu and Y. Fang, *Catal. Sci. Technol.*, 2014, **4**, 14-25.

15. P. Maitarad, D. S. Zhang, R. H. Gao, L. Y. Shi, H. R. Li, L. Huang, T. Rungrotmongkol and J. P. Zhang, *J. Phys. Chem. C*, 2013, **117**, 9999-10006.

16. C. Z. Wang, S. J. Yang, H. Z. Chang, Y. Peng and J. H. Li, *J. Mol. Catal. A*, 2013, **376**, 13-21.

17. X. Jiang, P. Lu, C. T. Li, Z. Zeng, G. M. Zeng, L. P. Hu, L. Mai and Z. Li, *Environ. Technol.*, 2013, **34**, 591-598.

18. J. Kim, A. Jentys, S. M. Maier and J. A. Lercher, *J. Phys. Chem. C*, 2013, **117**, 986-993.

19. S. X. Cai, D. S. Zhang, L. Zhang, L. Huang, H. R. Li, R. H. Gao, L. Y. Shi and J. P. Zhang, *Catal. Sci. Technol.*, 2014, **4**, 93-101.

20. F. Ayaria, M. Mhamdia, J. Álvarez-Rodríguezb, A. R. G. Ruizb, G. Delahayc and A. Ghorbela, *Appl. Catal., B*, 2013, **134**, 367-380.

21. G. J. Dong, Y. M. Li, Y. G. Wang, J. Zhang and R. R. Duan, *Reac. Kinet. Mech. Cat.*, 2014, **111**, 235-245.

22. B. Thirupathi and P. G. Smirniotis, *J. Catal.*, 2012, **288**, 74-83.

23. E. Park, M. Kim, H. Jung, S. Chin and J. Jurng, *ACS Catal.*, 2013, **3**, 1518-1525.

24. S. J. Yang, Y. W. Fu, Y. Liao, S. C. Xiong, Z. Qu, N. Q. Yan and J. H. Li, *Catal. Sci. Technol.*, 2014, **4**, 224-232.

25. L. Schill, R. Fehrmann, S. S. R. Putluru and A. D. Jensen, *Catal. Lett.*, 2014, **144**, 395-402.

26. J. Han, D. S. Zhang, P. Maitarad, L. Y. Shi, S. X. Cai, H. R. Li, L. Huang and J. P. Zhang, *Catal. Sci. Technol.*, 2014, **5**, 438-446.

27. Z. B. Wu, R. B. Jin, Y. Liu and H. Q. Wang, *Catal. Commun.*, 2008, **9**, 2217-2220.

28. D. S. Zhang, L. Zhang, L. Y. Shi, C. Fang, H. R. Li, R. H. Gao, L. Huang and J. P. Zhang, *Nanoscale*, 2013, **5**, 1127-1136.

29. L. Zhang, L. Y. Shi, L. Huang, J. P. Zhang, R. H. Gao and D. S. Zhang, *ACS Catal.*, 2014, **4**, 1753-1763.

30. K. Li, X. L. Tang, H. H. Yi, P. Ning, D. J. Kang and C. Wang, *Chem. Eng. J.*, 2012, **192**, 99-104.

31. M. Kobayashi and K. Miyoshi, *Appl. Catal., B*, 2007, **72**, 253-261.

32. M. Valencia, E. López, S. Andrade, M. L. Iris, V. RicoPérez, C. S. d. Lecea and A. BuenoLópez, *Catal. Commun.*, 2014, **46**, 86-89.

33. E. García-Bordejé, M. J. Lázaro, R. Moliner, J. F. Galindo, J. Sotres and A. M. Baró, *J. Catal.*, 2004, **223**, 395-403.

34. Y. Shu, T. Aikebaier, X. Quan, S. Chen and H. T. Yu, *Appl. Catal., B*, 2014, **150-151**, 630-635.

35. H. R. Li, D. S. Zhang, P. Maitarad, L. Y. Shi, R. H. Gao, J. P. Zhang and W. G. Cao, *Chem. Commun.*, 2012, **48**, 10645-10647.

36. S. X. Cai, D. S. Zhang, L. Y. Shi, J. Xu, L. Zhang, L. Huang, H. R. Li and J. P. Zhang, *Nanoscale*, 2014, **6**, 7346–7353.

37. S. He, Y. F. Zhao, M. Wei, D. G. Evans and X. Duan, *Ind. Eng. Chem. Res.*, 2012, **51**, 285-291.

38. J. Yao, J. S. Choi, K. S. Yang, D. Z. Sun and J. S. Chung, *Korean J. Chem. Eng.*, 2006, **23**, 888-895.

39. L. Yu, G. Q. Zhang, C. Z. Yuan and X. W. Lou, *Chem. Commun.*, 2013, **49**, 137-139.

40. Y. S. Luo, J. S. Luo, J. Jiang, W. W. Zhou, H. P. Yang, X. Y. Qi, H. Zhang, H. J. Fan, D. Y. W. Yu, C. M. Li and T. Yu, *Energ Environ. Sci.*, 2012, **5**, 6559-6566.

41. Z. Ren, Y. B. Guo, Z. H. Zhang, C. H. Liu and P. X. Gao, *J. Mater. Chem. A*, 2013, **1**, 9897-9906.

42. Y. Li and W. J. Shen, *Chem. Soc. Rev.*, 2014, **43**, 1543-1574.

43. X. J. Du, D. S. Zhang, R. H. Gao, L. Huang, L. Y. Shi and J. P. Zhang, *Chem. Commun.*, 2013, **49**, 6770-6772.

44. Z. Q. Sun, J. H. Kim, Y. Zhao, F. Bijarbooneh, V. Malgras, Y. Lee, Y. M. Kang and S. X. Dou, *J. Am. Chem. Soc.*, 2011, **133**, 19314-19317.

45. J. J. Xue, X. Q. Wang, G. S. Qi, J. Wang, M. Q. Shen and W. Li, *J. Catal.*, 2013, **297**, 56-64.

46. B. X. Shen, Y. Y. Wang, F. M. Wang and T. Liu, *Chem. Eng. J.*, 2014, **236**, 171-180.

47. D. S. Zhang, L. Zhang, L. Y. Shi, C. Fang, H. R. Li, R. H. Gao, L. Huang and J. P. Zhang, *Nanoscale*, 2013, **5**, 1127-1136.

48. L. Zhang, D. S. Zhang, J. P. Zhang, S. X. Cai, C. Fang, L. Huang, H. R. Li, R. H. Gao and L. Y. Shi, *Nanoscale*, 2013, **5**, 9821-9829.

49. G. Q. Zhang, H. B. Wu, H. E. Hoster, M. B. Chan-Par and X. W. Lou, *Energ. Environ. Sci.*, 2012, **5**, 9453-9456.

50. F. D. Liu, H. He, Y. Ding and C. B. Zhang, *Appl. Catal., B*, 2009, **93**, 194-204.

51. Z. H. Chen, Q. Yang, H. Li, X. H. Li, L. F. Wang and S. C. Tsang, *J. Catal.*, 2010, **276**, 56-65.

52. Z. Z. Zhu, G. Z. Lu, Z. G. Zhang, Y. Guo, Y. L. Guo and Y. Q. Wang, *ACS Catal.*, 2013, **3**, 1154-1164.

53. B. Zhao, X. K. Ke, J. H. Bao, C. L. Wang, L. Dong, Y. W. Chen and H. L. Chen, *J. Phys. Chem. C*, 2009, **113**, 14440–14447.

54. S. PalDey, S. Gedevanishvili, W. Zhang and F. Rasouli, *Appl. Catal., B*, 2005, **56**, 241-250.

55. S. Roy, B. Viswanath, M. S. Hegde and G. Madras, *J. Phys. Chem. C*, 2008, **112**, 6002-6012.

56. Z. H. Lian, F. D. Liu, H. He, X. Y. Shi, J. S. Mo and Z. B. Wu, *Chem. Eng. J*, 2014, **250**, 390-398.

57. B. Thirupathi and P. G. Smirniotis, *Appl. Catal., B*, 2011, **110**, 195-206.

58. X. L. Mou, B. S. Zhang, Y. Li, L. D. Yao, X. J. Wei, D. S. Su and W. J. Shen, *Angew. Chem. Int. Ed.* , 2012, **51**, 2989-2993.